




**Elastic scattering and boron, lithium, and  $\alpha$ -particle production in the  ${}^9\text{Be} + {}^{51}\text{V}$  reaction**H. Kumawat <sup>1,2,\*</sup>, M. Prasanna,<sup>3</sup> V. V. Parkar <sup>1,2</sup>, C. Joshi,<sup>4</sup> A. Kundu,<sup>5</sup> A. Pal,<sup>1</sup> K. Ramachandran,<sup>1</sup> D. Dutta,<sup>1,2</sup> S. Santra,<sup>1,2</sup> and S. Kailas <sup>6</sup><sup>1</sup>*Nuclear Physics Division, Bhabha Atomic Research Centre, Mumbai 400085, India*<sup>2</sup>*Homi Bhabha National Institute, Anushaktinagar, Mumbai 400094, India*<sup>3</sup>*Department of Physics, Rani Channamma University, Belagavi 591156, India*<sup>4</sup>*Department of Physics, The M. S. University of Baroda, Vadodara 390002, India*<sup>5</sup>*Department of Nuclear and Atomic Physics, Tata Institute of Fundamental Research, Mumbai 400005, India*<sup>6</sup>*UM-DAE Centre for Excellence in Basic Sciences, Mumbai 400098, India*

(Received 17 March 2022; accepted 21 July 2022; published 4 August 2022)

**Background:** Experimental and theoretical investigation of breakup coupling effects due to different cluster structures ( ${}^8\text{Be} + n$  and  ${}^5\text{He} + \alpha$ ), relative importance of neutron or  ${}^5\text{He}/\alpha$  transfer, and their contribution to  $\alpha$  production are important to understand reaction mechanism in a weakly bound projectile ( ${}^9\text{Be}$ ) near the Coulomb barrier.

**Purpose:** Breakup coupling effect on elastic scattering and measurement of angular distributions and energy spectra of  $\alpha$  particles produced through breakup, transfer, and complete fusion processes to disentangle their relative contributions and to investigate the relative importance of breakup followed by fusion (breakup-fusion) are compared to transfer.

**Methods:** Elastic scattering, inclusive  $\alpha$  production, lithium, and boron production cross sections have been measured for the  ${}^9\text{Be} + {}^{51}\text{V}$  system above Coulomb barrier energies. Continuum-discretized-coupled-channels (CDCC) breakup coupling effect using  ${}^8\text{Be} + n$  and  ${}^5\text{He} + \alpha$  cluster configurations have been investigated. Coupled reaction channels (CRC) calculations for  $1p$ ,  $1d$ , and  $1n$  stripping and  $1p$ ,  $1d$  pickup leading to  ${}^8\text{Li} + {}^{52}\text{Cr}$ ,  ${}^7\text{Li} + {}^{53}\text{Cr}$ ,  ${}^8\text{Be} + {}^{52}\text{V}$ , and  ${}^{10}\text{B} + {}^{50}\text{Ti}$ ,  ${}^{11}\text{B} + {}^{49}\text{Ti}$ , respectively, were performed and compared with the experimental data. Theoretical calculations for the estimation of various reaction channels contributing to  $\alpha$  production have been performed with CDCC and CRC methods using the FRESKO code.

**Results:** Global optical model parameters for the  ${}^9\text{Be}$  projectile describe the elastic scattering data very well and the optical model fit improves the  $\chi^2$  slightly. CRC calculations show a major contribution in the production of lithium through  $1p$ ,  $1d$  stripping and boron through  $1p$ ,  $1d$  pickup reactions.  $\alpha$  production angular and energy distributions are obtained, and direct  $\alpha$  production is described with contributions from noncapture breakup, breakup-fusion, and transfer reactions.

**Conclusions:** Breakup coupling for  ${}^5\text{He} + \alpha$  and  ${}^8\text{Be} + n$  cluster structures shows a repulsive and attractive coupling effect on elastic scattering, respectively. The  ${}^8\text{Be} + n$  cluster structure also shows a dipole polarization effect by suppressing the Coulomb rainbow compared to the  ${}^5\text{He} + \alpha$  cluster structure. Kinematic analysis of the  $\alpha$  particles energy spectra suggest that  $\alpha$  production is dominated by breakup-fusion over cluster transfer. CRC calculations suggest that  $1p$ ,  $1d$  stripping and pickup reactions are a major contributor to lithium and boron production cross sections.

DOI: [10.1103/PhysRevC.106.024602](https://doi.org/10.1103/PhysRevC.106.024602)**I. INTRODUCTION**

Experimental and theoretical studies of the reaction mechanism with weakly bound nuclei have been done in the last several years [1,2]. Weakly bound halo nuclei, such as  ${}^6,8\text{He}$ ,  ${}^{11}\text{Li}$ ,  ${}^{11}\text{Be}$ , have a very high probability of breakup and have diffused density distributions. Weakly bound stable nuclei, i.e.,  ${}^6,7\text{Li}$ ,  ${}^9\text{Be}$ , mimic similar behavior in reaction mechanisms, like rare ion beams (RIB), and are easy to study due to higher beam intensities. Because of the loosely bound nature,

breakup coupling to a continuum suppresses fusion above barrier energies and enhancement in the fusion cross section is seen below the barrier due to coupling to bound channels which leads to lower fusion barrier [3–14]. In the case of  ${}^9\text{Be}$ , the prompt and delayed noncapture breakup are difficult to identify experimentally due to two similar  $\alpha$  particles as breakup fragments. The complete fusion suppression for  ${}^6,7\text{Li}$  is reported to be independent of the target mass except for a lighter mass region where CF and ICF are difficult to separate [15,16]. The suppression factor is inversely proportional to the breakup threshold energy above the Coulomb barrier and the enhancement below barrier energies has an effect of target structure [13].

\*harphool@barc.gov.in

There are three types of measurements to investigate a reaction mechanism with weakly bound nuclei: a) elastic scattering for the study of potential behavior near the Coulomb barrier, b) complete fusion (CF) and incomplete fusion (ICF) studies to investigate fusion suppression or enhancement, and c) inclusive and exclusive  $\alpha$  production to investigate contributions of direct reaction channels. The reaction cross section and optical potential parameters are deduced from elastic scattering measurements. The parameters are used to calculate the cross sections for the transfer and breakup channels and coupling effects on elastic and fusion measurements. The continuum-discretized-coupled-channels (CDCC) method is successfully used to study the breakup coupling effect on the reaction mechanism. The  $^9\text{Be}$  projectile has very close breakup thresholds for  $^9\text{Be} \rightarrow ^8\text{Be} + n$ , 1.67 MeV and  $^9\text{Be} \rightarrow ^5\text{He} + ^4\text{He}$ , 2.46 MeV channels. Due to its Borromean structure  $^9\text{Be}$  can also break into  $2\alpha + n$  (1.57 MeV). Three- and four-body CDCC calculation methods are used to describe the elastic scattering and breakup data [17,18]. A large number of studies were performed with  $^9\text{Be}$ , weakly bound projectile, to have a better understanding of the breakup influence on elastic scattering [4,9,11,19,20]. While no breakup influence was observed for light and medium mass targets [9], a repulsive nature for  $^5\text{He} + ^4\text{He}$  breakup and an attractive nature was reported for the  $^8\text{Be} + n$  breakup coupling [14,21] for medium mass targets. A dipole polarization effect on elastic scattering was reported by Alvarez *et al.* [22] for  $^6\text{He}$ ,  $^9\text{Be}$ ,  $^{11}\text{Li}$ , and  $^{11}\text{Be}$  projectiles.

Large  $\alpha$  production cross sections are observed due to ICF, transfer, and breakup in weakly bound projectiles [23,24]. Integral  $\alpha$  production cross section, angular, and energy distributions provide challenges to present a reaction theory to disentangle different sources of  $\alpha$  production. The exclusive particle- $\gamma$  measurements have a strong dependence of coincidence efficiency on detector geometry [25]. The coincidence measurements between particle and  $\gamma$  rays from residues help to understand CF and ICF contributions. The minor channels are difficult to measure in exclusive measurements. The estimation of ICF contribution is not free from model calculations as in many cases the same residue is populated by CF and ICF channels. It becomes further complicated as ICF residues can emit particles if populated to higher excited states. The inclusive spectra measure full production cross sections comprised of major and minor channels. The direct  $\alpha$  cross sections are not free from model parameters as the compound nuclear contribution is based on model calculations, although the model parameters are fixed by measuring  $\alpha$  spectra at large angles where the compound nuclear contribution is dominated. The inclusive spectra give us a chance to calculate minor channels to supplement exclusive measurements in understanding the reaction mechanism.

The energy spectra of projectile-like fragments and, in particular,  $\alpha$  particles can reveal a lot about their origin. Apart from noncapture breakup, breakup fusion and transfer are major sources of  $\alpha$  particle production. If the positive  $Q$  value is shared with the outgoing  $\alpha$  particle then it contributes to high energy  $\alpha$  production (cluster transfer) but in the case of breakup fusion (breakup followed by fusion), the  $\alpha$  particles do not get extra energy from the positive  $Q$  value and peak

near projectile velocity. Do these energy spectra depend on the specific projectile, target, or excitation energy? Several reports [21,26] have done exclusive and inclusive measurements to find the solution of this open question of various contributions to inclusive  $\alpha$  production. In the case of the  $^6\text{Li}$  ( $E = 2.4V_b$ ) +  $^{197}\text{Au}$  system,  $\alpha$ - $\gamma$  coincidence measurements suggest at least 13% contribution coming from a transfer reaction where the  $Q$  value was shared but a major peak was observed at projectile velocities [27]. Theoretical studies could explain  $\alpha$  production from the breakup-fusion mechanism for the  $^7\text{Li}$  case [23,28]. The  $\alpha$  energy spectrum from an exclusive measurement for the  $^7\text{Li}$  ( $E = 1.3V_b$ ) +  $^{93}\text{Nb}$  system [29] and  $^7\text{Li}$  ( $E = 1.2V_b$ ) +  $^{209}\text{Bi}$  [30] observed that the cluster transfer is dominant ( $\approx 70\%$  for  $^{93}\text{Nb}$ ) and peak energy is much higher than projectile velocities while other studies have suggested a mechanism of breakup fusion to be more important [31]. Another, exclusive and inclusive measurement for  $^7\text{Li}$  ( $E = 3V_b$ ) +  $^{159}\text{Tb}$  observed that the  $\alpha$  particle energy spectra peak around projectile velocities. There were differences in target mass ( $^{93}\text{Nb}$  is lighter mass target) and projectile energies in these measurements. Is the difference due to target mass or energy? The inclusive measurement for lighter mass target ( $^7\text{Li}$  ( $E = 3.4V_b$ ) +  $^{58}\text{Ni}$  [32]) reported the major peak at projectile velocities, hence no conclusion can be drawn for its dependence on mass and energy. The measurement for  $^9\text{Be}$  ( $E = 1.7V_b$ ) +  $^{28}\text{Si}$  [10] observed a major peak around projectile velocity.

In the present work, the elastic scattering, energy, and angular distributions of inclusive  $\alpha$ , angular distributions of lithium and boron for the  $^9\text{Be}$  ( $E = 1.6 - 1.7V_b$ ) +  $^{51}\text{V}$  system are reported. Kinematic analyses of  $\alpha$  energy spectra were performed to understand the dominant processes. Theoretical calculations for breakup and various transfer channels are performed to interpret the experimental data. The results manifest contributions from breakup and transfer channels. The article is organized as follows. Section II is dedicated to experimental details. Section III describes the data reduction procedure for  $\alpha$  energy and angular distributions. Kinematic analysis for the origin of  $\alpha$  particles by different processes is discussed in Sec. IV. Theoretical analysis using the statistical model, CDCC, CRC calculations for  $1n$ ,  $1p$ , and  $1d$  stripping, and  $1p$ ,  $1d$  pickup using FRESKO are described in Sec. V. Summary is given in Sec. VI.

## II. EXPERIMENTAL DETAILS

An experiment was performed at the 14 UD BARC-TIFR Pelletron-Linac accelerator facility, Mumbai, India with a  $^9\text{Be}^{4+}$  beam at energies of 26 and 28 MeV. The beam was incident on a self-supported  $^{51}\text{V}$  target of thickness 1.17 mg/cm<sup>2</sup>. Beam energies were corrected for the energy loss in the half-target thickness and the corrected energies were 25.3 and 27.3 MeV, respectively. The detection system consisted of a set of ten solid state silicon surface barrier telescope detectors in  $\Delta E + E$  arrangement and two monitors at  $\pm 10^\circ$  for absolute normalization. The angles covered by telescope detectors were  $10^\circ$  to  $70^\circ$  in the laboratory frame. The data were recorded using the Linux based data acquisition system, LAMPS [33]. A typical measured  $\Delta E - E_{\text{tot}}$  two-dimensional

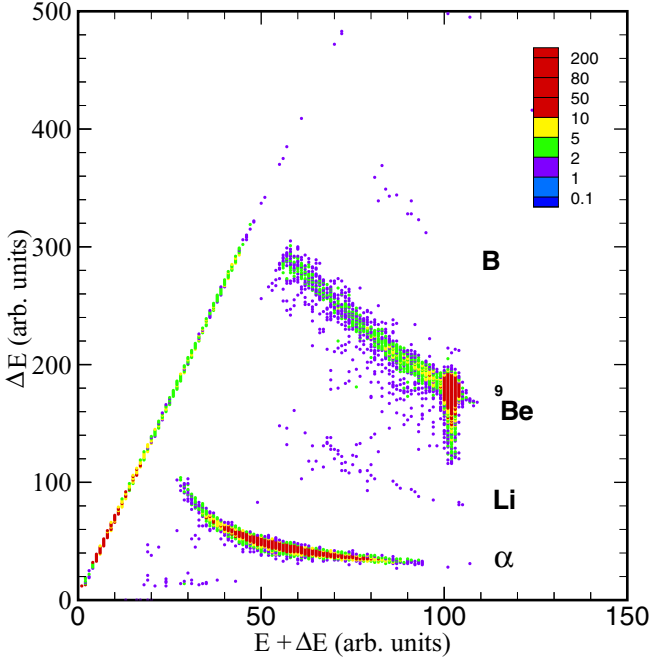


FIG. 1. The typical biparametric  $\Delta E - E_{\text{tot}}$  plot for the  ${}^9\text{Be} + {}^{51}\text{V}$  system at  $E_{\text{lab}} = 27.3$  MeV,  $\theta_{\text{lab}} = 40^\circ$ .

plot at  $E_{\text{lab}} = 27.3$  MeV and  $\theta_{\text{lab}} = 40^\circ$  is given in Fig. 1 which shows  $\alpha$ , lithium,  ${}^9\text{Be}$ , and boron bands. The counts for lithium and boron were very small and statistical errors were from 15% to 40%. The particle identification (PI) plot suggests  ${}^{7,8}\text{Li}$  and  ${}^{10,11}\text{B}$  in the lithium and boron bands but it was not possible to resolve them due to low statistics so total counts for lithium and boron are extracted to get the angular distributions.

### III. EXPERIMENTAL ENERGY AND ANGULAR DISTRIBUTIONS

The elastic scattering angular distributions were measured and shown in Fig. 2. A monitor detector was used for normalization and to get the ratio with Rutherford cross sections. The elastic angular distribution data were used to get  $\alpha$  energy and angular distributions as explained below. The  $\alpha$  particles were produced by  ${}^9\text{Be}$  noncapture elastic breakup,  ${}^8\text{Be}$  breakup following neutron transfer,  $\alpha/{}^5\text{He}$  transfer, ICF, and CF processes. The energy spectra from  $\theta_{\text{lab}} = 20^\circ$  to  $65^\circ$  (grazing angles  $\approx 41^\circ, 46^\circ$ ), are shown in Fig. 3 for 27.3 and 25.3 MeV energies. The experimental energy spectra include  $\alpha$  particles originating from both direct and compound nuclear reactions. The energy spectra show a dominant contribution from direct reactions compared to the compound nuclear reactions near grazing angles.

The energy integrated  $\alpha$  particle yields were obtained at different angles and angular distributions were obtained using the following equation [34]:

$$\frac{d\sigma_\alpha}{d\Omega} = \frac{Y_\alpha}{Y_{el}} \times \frac{d\sigma_{el}}{d\Omega}. \quad (1)$$

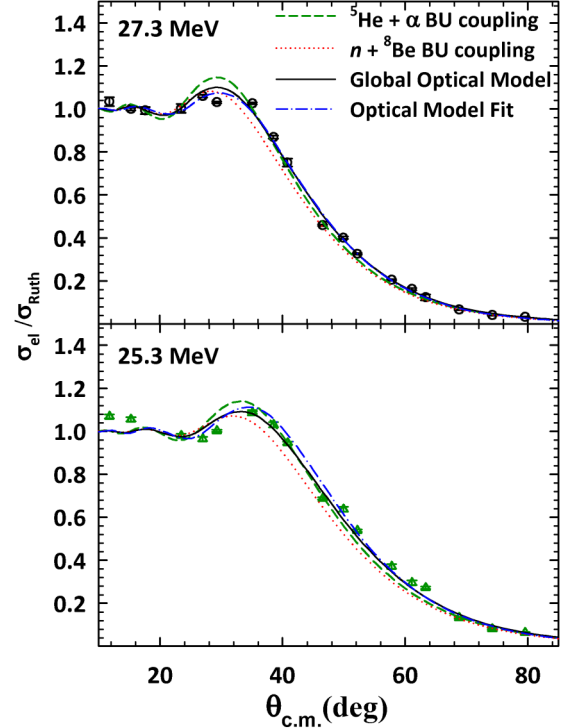


FIG. 2. Elastic scattering angular distribution for the  ${}^9\text{Be} + {}^{51}\text{V}$  system. The global optical model calculations are shown by solid lines, optical model fitted values are shown by dash-dotted lines, breakup coupling effects using CDCC for  $\alpha + {}^5\text{He}$  and  $n + {}^8\text{Be}$  clusters are given by dashed and dotted lines, respectively.

Here,  $Y_\alpha$ ,  $Y_{el}$  are  $\alpha$  particle and elastic scattering yields,  $d\sigma_{el}/d\Omega$  is the elastic scattering cross section, as given in Fig. 2. The  $\alpha$  cross section is comprised of direct and compound nuclear reactions. Direct  $\alpha$  cross sections can be obtained by subtracting the compound nuclear contribution from the total measured  $\alpha$  cross sections. The total  $\alpha$ -production angular distributions are shown in Fig. 4 along with compound nuclear, breakup, and transfer induced  $\alpha$  particles. It is clear that well above grazing angles the cross sections are dominated by the compound nuclear or CF reaction whereas breakup and transfer following  $\alpha$  particles peak near grazing angles. The angle integrated direct  $\alpha$  cross sections at projectile energies were obtained by fitting the Gaussian shape to  $(d\sigma/d\Omega) \times 2\pi \sin\theta$  distributions. Thus  $\alpha$  cross sections were deduced using the equation

$$\sigma_\alpha = \int_0^{2\pi} d\phi \int_0^\pi \frac{d\sigma_\alpha(\theta)}{d\Omega} \sin\theta d\theta. \quad (2)$$

The deduced experimental direct  $\alpha$  cross sections along with errors are given in Table I. The errors were obtained due to fitting errors in the three parameters (strength, mean, and width) of the Gaussian distributions. Maximum and minimum cross sections were obtained by adding these errors to the mean values of the parameters, and thus mean errors were deduced in the cross sections. A similar procedure was adopted to get experimental cross sections for Li ( $\sigma_{\text{Li}}^{\text{exp}}$ ) and B ( $\sigma_{\text{B}}^{\text{exp}}$ ) production and there were no contributions of compound

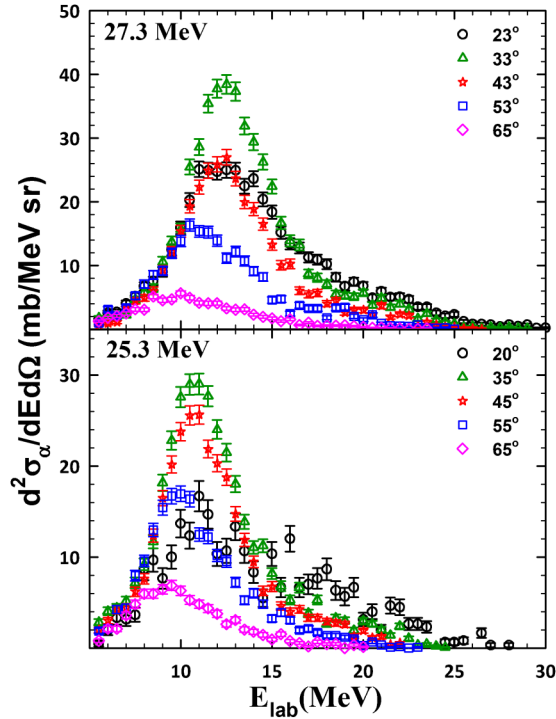


FIG. 3. Energy spectra of  $\alpha$  particles at  $E_{\text{lab}} = 27.3$  and  $25.3$  MeV from  $\theta_{\text{lab}} = 20^\circ$  to  $65^\circ$  for the  ${}^9\text{Be} + {}^{51}\text{V}$  system. The experimental data for total (direct + compound)  $\alpha$  production are presented.

nuclear reactions from PACE predictions for these channels. The average energies at  $E_{\text{lab}} = 27.3$  MeV for lithium were  $\approx 20, 17, 16.5,$  and  $16$  MeV at  $\theta_{\text{lab}} = 30^\circ, 40^\circ, 50^\circ,$  and  $60^\circ$ , respectively, and for boron  $\approx 24$  and  $21$  MeV at  $\theta_{\text{lab}} = 30^\circ, 40^\circ$ , respectively.

#### IV. KINEMATIC ANALYSIS OF $\alpha$ PARTICLE ENERGY SPECTRA

Kinematic analysis of the  $\alpha$  particle energy spectra was carried out and energy centroids ( $\bar{E}_\alpha = E_{\text{c.m.}} + Q_{\text{opt}}$ ) in the c.m. system were calculated using kinematics for different processes and are given in Table II. A leading order expression proposed by Schiffer for  $Q_{\text{opt}}$  was used which is given as  $E_{\text{c.m.}}(Z_3 Z_4 / Z_1 Z_2 - 1)$  [35], where  $Z_1, Z_2, Z_3, Z_4$  are the atomic numbers of the projectile, target, ejectile, and residual nucleus, respectively. The energy centroids of the elastic or noncapture breakups  ${}^8\text{Be}(2\alpha) + n$  and  $\alpha + {}^5\text{He}(\alpha + n)$  are close to the beam velocities as the breakup threshold energies

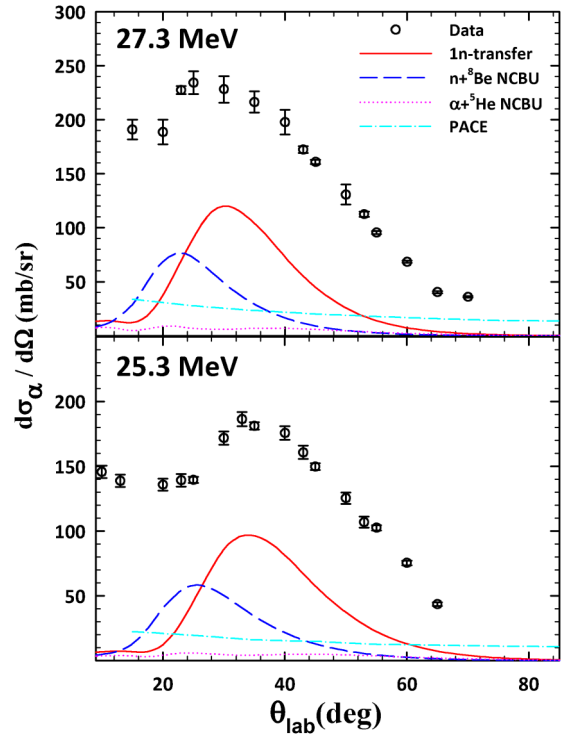


FIG. 4. Angular distributions of total  $\alpha$  production cross-sections at  $E_{\text{lab}} = 27.3$  and  $25.3$  MeV along with compound nuclear (dash-dotted lines),  $1n$ -transfer (solid lines),  $n + {}^8\text{Be}$  (dashed lines) non-capture breakup,  $\alpha + {}^5\text{He}$  (dotted lines) non-capture breakup contributions.

are very small. The breakup cross sections were calculated for resonant and continuum states using FRESKO and are given in Table I. Neutron transfer followed by the breakup of  ${}^8\text{Be}$  also gives two  $\alpha$  particles and the calculation details are given in Sec. V.

In the case of transfer reactions, if breakup followed by fusion takes place then energy from the  $Q$  value is not shared with the outgoing fragments like  ${}^8\text{Be}, \alpha,$  or  ${}^5\text{He}$  for neutron and  ${}^5\text{He}$  or  $\alpha$  transfer, respectively. The centroid energies in Table II are given for the cluster transfer where the energy from the  $Q$  value is not shared with the outgoing fragment.  $Q_{\text{opt}}$  for neutron transfer is taken as zero. In the case of the sharing of the  $Q$  value with the outgoing fragments, the following possibilities exist for the present study at  $27.3$  MeV

- (a) Neutron transfer: after neutron transfer, the emitted  ${}^8\text{Be}$  breaks into  $2\alpha$  particles which would peak around

TABLE I. Deduced experimental direct  $\alpha$  production ( $\sigma_\alpha^{\text{Direct}}$ ), Li and B production cross sections ( $\sigma_{\text{Li}}^{\text{exp}}, \sigma_{\text{B}}^{\text{exp}}$ ) obtained from integral of measured angular distributions, calculated cross sections for noncapture breakup ( $\sigma_{\alpha+{}^5\text{He}}^{\text{NCBU}}$  and  $\sigma_{n+{}^8\text{Be}}^{\text{NCBU}}$ ),  $1n$  stripping ( $\sigma_{-1n}^{\text{tr}}$ ),  $1p$  stripping ( $\sigma_{-1p}^{\text{tr}}$ ),  $1d$  stripping ( $\sigma_{-1d}^{\text{tr}}$ ), and  $1p, d$  pickup cross section by  $\sigma_{+1p,d}^{\text{pickup}}$ , CF cross sections from PACE are represented by  $\sigma_{\text{PACE}}^{\text{CF}}$ .

$E_{\text{lab}}$ MeV	$\sigma_\alpha^{\text{Direct}}$ (mb)	$\sigma_{\text{Li}}^{\text{exp}}$ (mb)	$\sigma_{\text{B}}^{\text{exp}}$ (mb)	$\sigma_{\alpha+{}^5\text{He}}^{\text{NCBU}}$ (mb)	$\sigma_{n+{}^8\text{Be}}^{\text{NCBU}}$ (mb)	$\sigma_{-1n}^{\text{tr}}$ (mb)	$\sigma_{-1p}^{\text{tr}}$ (mb)	$\sigma_{-1d}^{\text{tr}}$ (mb)	$\sigma_{+1p,d}^{\text{pickup}}$ (mb)	$\sigma_{\text{PACE}}^{\text{CF}}$ (mb)
27.3	$576 \pm 45$	$3.4 \pm 0.7$	$1.0 \pm 0.4$	28	38	93	0.21	1.7	0.5	944
25.3	$460 \pm 58$	$1.7 \pm 0.4$		27	36	89	0.20	1.4	0.4	850



TABLE II. Kinematic parameters for the  $\alpha$  transfer channel for the  ${}^9\text{Be} + {}^{51}\text{V}$  system.  $Q_{gg}$  represent the transfer to ground state, the optimum  $Q$  value ( $Q_{\text{opt}}$ ) is calculated at leading order according to Ref. [36], centroid energy of the direct  $\alpha$  for the respective channels in the c.m. system ( $\bar{E}_\alpha = E_{\text{c.m.}} + Q_{\text{opt}}$ ).  ${}^8\text{Be} \rightarrow 2\alpha$  and  ${}^5\text{He} \rightarrow \alpha + n$  are assumed to be broken by giving  $\alpha$  particles. The energies of breakup constituents are calculated as per mass ratio.

$E_{\text{c.m.}}$ (MeV)		$n$ trans. (MeV)	$\alpha({}^5\text{He})$ trans. (MeV)	$1n + {}^8\text{Be}$ (MeV)	$\alpha + {}^5\text{He}$ (MeV)
23.2	$Q_{gg}$	5.6	5.6(13.6)	-1.66	-2.46
	$Q_{\text{opt}}$	0.0	-10.6		
	$\bar{E}_\alpha$	11.6	10.7(12.6)	9.6	9.3
21.5	$Q_{\text{opt}}$	0.0	-9.8		
	$\bar{E}_\alpha$	10.7	10(11.7)	8.8	8.5

14 MeV. It is shown by a dashed line in Fig. 5. The relative area around this peak energy under the direct  $\alpha$  curve was obtained and angular distribution was extracted to get the integral cross section. The area was divided by factor of two as there are  $2\alpha$  in this channel. The cross section comes out to be  $87 \pm 11$  mb which is close to the calculated value.

- (b)  $\alpha$  transfer: the resulting  ${}^5\text{He}$  breaks into the neutron and  $\alpha$  particles which would peak around  $\approx 18$  MeV. In Fig. 5 this possible process is shown by dotted lines. The integral cross section by relative area around this peak was deduced and it was  $8 \pm 6$  mb.
- (c)  ${}^5\text{He}$  transfer: the resulting  $\alpha$  particles would peak around  $\approx 25$  MeV. Such high energy  $\alpha$  particles are not observed.

## V. THEORETICAL ANALYSIS

### A. Statistical model calculations

The contribution from the compound nuclear reaction for an  $\alpha$  production cross section was calculated using the sta-

tistical model code PACE [37]. The Ignatyuk prescription [38] of the level density with parameter ( $\bar{a} = A/10 \text{ MeV}^{-1}$ ,  $A = \text{mass number}$ ) was used which is similar to  ${}^6\text{Li} + {}^{51}\text{V}$  [39] and  ${}^9\text{Be} + {}^{93}\text{Nb}$  [21] systems. Variation in  $\bar{a}$  from  $A/8$  to  $A/11 \text{ MeV}^{-1}$  changes the relative evaporation of particles but not the position of the peak energy. The uncertainty in the deduced direct  $\alpha$ -cross sections due to PACE predictions is less than 10% and included in the experimental deduced values. The angular distributions of  $\alpha$  production due to the compound nucleus evaporation reaction are given in Fig. 4. The compound nuclear angular distributions show a resemblance well above grazing angles with the experimental data. The direct contributions peak near grazing angles  $\approx 41^\circ$  and  $46^\circ$  at 27.3 and 25.3 MeV, respectively.

### B. Phenomenological optical model calculations

An optical model analysis of the elastic scattering differential cross-section data has been performed using the SFRESKO module of the FRESKO code version FRES 3.3 [40]. The Woods-Saxon forms were used for both the real and imaginary parts and imaginary surface part of the optical potentials. Optical model calculations were performed with the global optical model potential parameters [41] which reproduces the data very well as shown in Fig. 2. The obtained reaction cross sections are given in Table III. These global potential parameters [41] were taken as initial parameters to obtain improved  $\chi^2$  values. In the first case, radius parameters ( $r_R, r_V, r_S$ ) were fixed but diffuseness ( $a_R, a_V, a_S$ ) and strength ( $V_R, W_V, W_S$ ) parameters were adjustable and in the second case, the strength ( $V_R, W_V, W_S$ ) parameters were adjustable and others were fixed. In both cases, the fit improves slightly and reaction cross sections vary  $\approx 5\%$ . The global, fitted parameters and the corresponding reaction cross sections are listed in Table III. The calculated elastic angular distributions using global and fitted parameters are shown in Fig. 2 with solid and dash-dotted lines.

### C. Continuum discretized coupled channel calculations

The noncapture or elastic breakup cross sections are calculated with CDCC using the code FRESKO version 3.3 [40,42]. The  ${}^9\text{Be}$  nucleus was assumed as a two-body  $\alpha + {}^5\text{He}$  and  $1n + {}^8\text{Be}$  clusters [14,21]. The continuum above the breakup threshold of  ${}^9\text{Be} \rightarrow \alpha + {}^5\text{He}$  (2.46 MeV) and  $1n + {}^8\text{Be}$  (1.66 MeV) were discretized into momentum bins of width  $\Delta k = 0.1 \text{ fm}^{-1}$ . The cluster resonant states were adopted from Ref. [43]. The continuum momentum bins were truncated at  $\epsilon_{\text{max}} = 7 \text{ MeV}$ . Each continuum or resonance state was further binned into 100 equal  $k$  bins. The relative orbital angular momentum  $L = 0, 1, \text{ and } 2$  were included in the calculations. In addition, the  $7/2^-$  (6.76 MeV) resonance for  $\alpha + {}^5\text{He}$  with experimental width was also included. The discretization is suitably modified to avoid double counting due to the resonances. The binding potential for the  $\alpha + {}^5\text{He}$  clusters were taken from Ref. [44]. The ground state of  ${}^9\text{Be}$  was constructed by taking the relative angular momentum  $L = 0, 2$  between the  ${}^5\text{He}$  (3/2) core and  $\alpha$  (0+) cluster. The  $L = 2$  component is taken in order to account for the

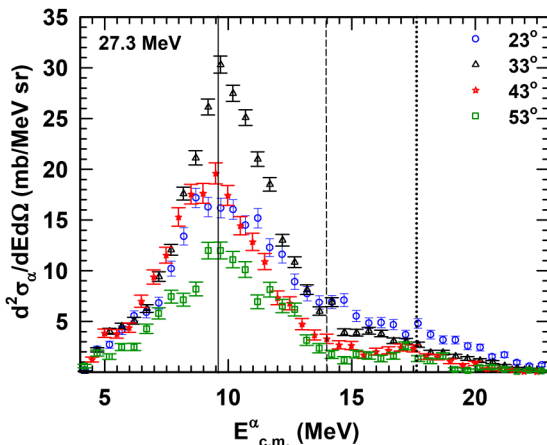


FIG. 5. Direct  $\alpha$  energy distribution at  $E_{\text{lab}} = 27.3 \text{ MeV}$  for various measured laboratory angles. Positions of breakup, neutron transfer and  $\alpha$  transfer is shown by solid, dashed and dotted lines, respectively.

TABLE III. Global optical model parameters and best fit optical potential parameters for the  ${}^9\text{Be} + {}^{51}\text{V}$  system from elastic scattering data, where the radius is given by  $R_i = A_T^{1/3}$  fm,  $R$ ,  $V$ ,  $S$  denote the real volume, imaginary volume, and surface type potentials, and  $N$  represents the number of data points

$E_{\text{lab}}$ MeV	$V_R$ MeV	$r_R$ fm	$a_R$ fm	$W_V$ MeV	$r_V$ fm	$a_V$ fm	$W_S$ MeV	$r_S$ fm	$a_S$ fm	$\sigma_R$ mb	$\chi^2/N$
Global parameters											
27.3	262.48	1.301	0.726	10.77	1.64	0.60	48.74	1.20	0.843	1267	2.0
25.3	262.94	1.301	0.726	10.20	1.64	0.60	48.99	1.20	0.843	1152	3.1
Best fit parameters											
27.3	268.4	1.301	0.694	1.0	1.64	0.50	18.81	1.20	1.0	1293	1.2
27.3	270.4	1.301	0.726	1.0	1.64	0.60	46.46	1.20	0.843	1246	1.3
25.3	271.1	1.301	0.703	8.8	1.64	1.00	1.25	1.20	1.0	1070	1.3
25.3	267.3	1.301	0.726	1.0	1.64	0.60	34.81	1.20	0.843	1065	2.1

reorientation of the highly deformed ( $\beta \approx 1.3$ )  ${}^9\text{Be}$  nucleus as given in Refs. [14,21]. The binding potential was allowed to adjust for the reproduction of the binding energy of the  ${}^9\text{Be}$  nucleus. The cluster folding potentials for  $\alpha + {}^{51}\text{V}$  and  ${}^5\text{He} + {}^{51}\text{V}$  at respective energies per mass ( $4/9$  of  $E_{\text{lab}}$  for  $\alpha$  and  $5/9$  of  $E_{\text{lab}}$  for  ${}^5\text{He}$ ) were generated from Ref. [45] and are given in Table IV.

In the second cluster structure of  ${}^9\text{Be} \rightarrow n + {}^8\text{Be}$ , the binding potential was taken from Ref. [46]. The resonant states,  $5/2^-$  (2.43 MeV),  $1/2^-$  (2.78 MeV),  $5/2^+$  (3.05 MeV), and  $3/2^+$  (4.70 MeV) were considered along with continuum bins. The  $n + {}^{51}\text{V}$  potential was taken from Ref. [47] and the  ${}^8\text{Be} + {}^{51}\text{V}$  potential was taken similar to  ${}^9\text{Be} + {}^{51}\text{V}$  [41] for scaled energy per mass and are given in Table IV. The breakup cross sections at different energies are given in Table I and angular distributions are plotted in Fig. 4. The  $\alpha + {}^5\text{He}$  coupling poorly describes the data at higher angles and the coupling generated an overall repulsive effect. In the case of  $n + {}^8\text{Be}$  clusters, the coupling produces an attractive effect and describes the data better at large angles.  $n + {}^8\text{Be}$  coupling suppresses the Coulomb rainbow while in the case of  $\alpha + {}^5\text{He}$  coupling a Coulomb rainbow is present. The Coulomb dipole polarization effect was also shown by Alvarez *et al.* [22] for various weak and exotic nuclei.

#### D. $1n$ stripping

The  $1n$  transfer followed by the breakup of  ${}^8\text{Be} \Rightarrow 2\alpha$  can contribute to  $\alpha$  production. The CRC calculations of  $1n$  transfer resulted in a considerable contribution to inclusive  $\alpha$  cross section by the reaction  ${}^{51}\text{V}({}^9\text{Be}, {}^8\text{Be}){}^{52}\text{V}$ . The Woods-Saxon

form factors were used with reduced radii  $r_0 = 1.25$  fm and diffuseness  $a = 0.65$  fm, for projectile as well as target bound state potentials. The spin-orbit interaction was included with a depth of 6 MeV. The depth of the real potential was allowed to vary to reproduce experimental neutron binding energies. The finite range transfer approximation in FRESKO [42] was used for the calculations in the post form. Full complex remnant terms were used with a two-way coupling scheme. The other important parameter, the spectroscopic factor for the projectile, was taken from Ref. [46]. The  $2^+(3.03$  MeV) resonance state was considered with the spectroscopic factor taken as one. The spectroscopic factors for the target were incorporated from the work of Karban *et al.* [48]. The calculations were performed for single  $n$  transfer to the  $2p_{3/2}$ ,  $1f_{5/2}$ ,  $2p_{1/2}$ , and  $1g_{9/2}$  orbits of available model space of  ${}^{52}\text{V}$  with the assumption of closure of the  $1f_{7/2}$  subshell in the ground state. The cross sections of  $1n$  stripping are given in Table I.

#### E. $1p$ , $1d$ stripping

In order to study the  $1p$  stripping contribution of the reaction  ${}^{51}\text{V}({}^9\text{Be}, {}^8\text{Li}){}^{52}\text{Cr}$ , CRC calculations have been performed. The calculations were performed for single  $p$  transfer to the  $1f_{7/2}$ ,  $2p_{3/2}$  orbits in the model space of  ${}^{52}\text{Cr}$ . The spectroscopic factors for the target were taken from Ref. [49]. The  ${}^9\text{Be}/{}^8\text{Li}$  overlapping spectroscopic factor was taken from Ref. [50] and the optical potential for  ${}^8\text{Li}$  was similar to the  ${}^7\text{Li}$  global optical potential [51]. The  $1p$  transfer cross sections are mentioned in Table I.

The CRC calculations have been performed for  $1d$  stripping or transfer contribution through the reaction  ${}^{51}\text{V}({}^9\text{Be},$

TABLE IV. Interaction potentials with the  ${}^{51}\text{V}$  target for CDCC calculations. Radius is given by  $R = (A_p^{1/3} + A_T^{1/3})$  fm.  $R$ ,  $V$ ,  $S$  denote real volume, imaginary volume, and surface type potentials.

Fragment	$V_R$ MeV	$r_R$ fm	$a_R$ fm	$W_V$ MeV	$r_V$ fm	$a_V$ fm	$W_S$ MeV	$r_S$ fm	$a_S$ fm	$\sigma_{R,27.3}^{\text{CDCC}}$ mb	$\sigma_{R,25.3}^{\text{CDCC}}$
$\alpha$	137.9	0.927	0.656	5.4	0.938	0.50	21.8	1.064	0.455	1278	1167
${}^5\text{He}$	130.0	0.930	0.637	8.7	0.917	0.50	17.5	1.040	0.455		
$n$	51.1	1.194	0.670	0.34	1.194	0.670	6.0	1.283	0.536	1453	1342
${}^8\text{Be}$	263.2	1.301	0.726	9.9	1.640	0.60	49.1	1.20	0.843		

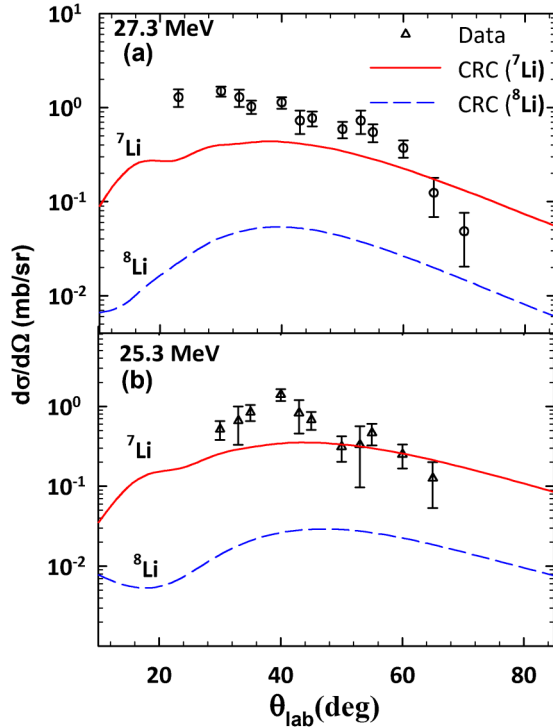


FIG. 6. Lithium production angular distribution for the  ${}^9\text{Be} + {}^{51}\text{V}$  system at (a) 27.3 MeV and (b) 25.3 MeV projectile energies. The  ${}^7\text{Li}$ ,  ${}^8\text{Li}$  production by  $1p$ ,  $1d$  stripping CRC calculated values are represented by solid and dashed lines, respectively. The calculated values have a major contribution from  ${}^7\text{Li}$  production.

${}^7\text{Li}$ )  ${}^{53}\text{Cr}$ . The calculations were performed for single  $d$  transfer to the  $1f_{7/2}$ ,  $2p_{3/2}$  orbits in the model space of  ${}^{53}\text{Cr}$ . The deuteron cluster was assumed to be in the  $S = 1$  state with no internal motion ( $n = 0$ ,  $l = 0$ ) for these nucleons. The quantum numbers ( $N$ ,  $L$ ) of the cluster in the center-of-mass motion were restricted to satisfy the harmonic-oscillator energy conservation relation

$$2(N - 1) + L = \sum_{i=1,2} 2(n_i - 1) + l_i, \quad (3)$$

where  $(n_i, l_i)$  are the quantum numbers of the individual nucleons of the deuteron cluster. The initial and final bound-state wave functions were calculated in a Woods-Saxon potential well with  $R = 1.2(A_{\text{core}} + A_{\text{cluster}})^{1/3}$  fm,  $a = 0.65$  fm and the depth of the potential was adjusted to reproduce the deuteron binding energy. The transition potential is the same as that responsible for binding the deuteron to the core. Also included in the calculations are the full “remnant” terms which are due to the difference in the core-core interaction. The spectroscopic factors for the target were taken as one. The  $1d$  transfer cross sections are mentioned in Table I and the angular distribution for  $1d$  and  $1p$  stripping are compared with the experimental data (see Fig. 6). All the CRC results presented here are without any normalization factor. The measurement and CRC calculated angular distributions agree qualitatively.

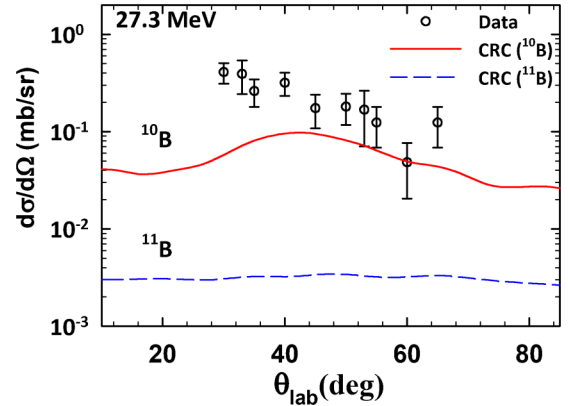


FIG. 7. Boron production angular distribution for the  ${}^9\text{Be} + {}^{51}\text{V}$  system at 27.3 MeV. The CRC calculated values for  ${}^{10,11}\text{B}$  production or  $1p + 1d$  pickup are represented by solid and dashed lines, respectively. The calculated values have a significant contribution for  ${}^{10}\text{B}$  production.

### F. $1p$ , $1d$ pickup

The CRC calculations were performed for  $1p$  and  $1d$  pickup reaction resulting in  ${}^{10}\text{B}$  and  ${}^{11}\text{B}$  as outgoing projectile-like fragments. The overlapping spectroscopic factors for  ${}^9\text{Be}/{}^{10}\text{B}$  ground and excited states were taken from [52] and taken as one for the  ${}^9\text{Be}/{}^{11}\text{B}$  overlap. Optical potential for  ${}^{10}\text{B} + {}^{50}\text{Ti}$  and  ${}^{11}\text{B} + {}^{49}\text{Ti}$  were taken from [51,53]. The calculated  $1d$  pickup cross section ( $\approx 0.03$  mb) was negligible compared to the  $1p$  pickup cross section ( $\approx 0.5$  mb at 27.3 MeV and  $\approx 0.4$  mb at 25.3 MeV). Experimentally, it was not possible to separate  ${}^{10,11,12}\text{B}$  hence boron cross sections are reported in Table I and plotted in Fig. 7 which are in good qualitative agreement with calculate values. It was not possible to extract the experimental data at 25.3 MeV.

## VI. SUMMARY

In summary, elastic scattering, inclusive  $\alpha$  production, lithium, and boron production cross sections have been measured for the  ${}^9\text{Be} + {}^{51}\text{V}$  system above the Coulomb barrier over a wide angular range and large  $\alpha$  particle yields were observed. The global optical potential for the  ${}^9\text{Be}$  projectile could reproduce the elastic scattering data, and the optical model fit improved the results slightly. Statistical model calculations have been performed to estimate the compound nuclear contributions in the  $\alpha$  particle production to obtain  $\alpha$  contributions from direct reactions. Noncapture breakup calculations using the CDCC method and CRC calculations for  $n$ ,  $p$ , and  $d$  transfer calculations were performed to estimate the contribution from these channels to  $\alpha$  production. The kinematic disentanglement of  $\alpha$  particles suggests that the majority of  $\alpha$  particles are close to beam velocity and breakup fusion is dominant compared to cluster transfer at these projectile energies. Qualitative agreement for angular distributions for the production of lithium and boron with CRC calculated values is observed and mean energies suggest direct stripping and pickup nature

for these fragments. More experiments with higher statistics and with other targets are required to better understand these processes.

### ACKNOWLEDGMENTS

The authors thank the BARC/TIFR Pelletron staff for excellent delivery of the beam and the support of the Department of Atomic Energy, Government of India, under Project

no. 12P-R&D-TFR-5.02-0300. Thanks are due to Dr. V. Jha for helping in CDCC calculations. One of the authors (C.J.) would like to acknowledge Department of Science and Technology (DST), Government of India for awarding her the Inspire Fellowship. The authors V.V.P. and S.K. acknowledge the financial support from the Young Scientist Research grant and Senior Scientist program, respectively, from the Indian National Science Academy (INSA), Government of India, in carrying out these investigations.

- 
- [1] B. B. Back, H. Esbensen, C. L. Jiang, and K. E. Rehm, *Rev. Mod. Phys.* **86**, 317 (2014).
- [2] L. Canto, P. Gomes, R. Donangelo, and M. Hussein, *Phys. Rep.* **424**, 1 (2006).
- [3] C. S. Palshetkar, S. Santra, A. Chatterjee, K. Ramachandran, S. Thakur, S. K. Pandit, K. Mahata, A. Shrivastava, V. V. Parkar, and V. Nanal, *Phys. Rev. C* **82**, 044608 (2010).
- [4] P. R. S. Gomes, I. Padron, E. Crema, O. A. Capurro, J. O. Fernandez Niello, A. Arazi, G. V. Marti, J. Lubian, M. Trotta, A. J. Pacheco, J. E. Testoni, M. D. Rodriguez, M. E. Ortega, L. C. Chamon, R. M. Anjos, R. Veiga, M. Dasgupta, D. J. Hinde, and K. Hagino, *Phys. Rev. C* **73**, 064606 (2006).
- [5] N. T. Zhang, Y. D. Fang, P. R. S. Gomes, J. Lubian, M. L. Liu, X. H. Zhou, G. S. Li, J. G. Wang, S. Guo, Y. H. Qiang, Y. H. Zhang, D. R. Mendes Junior, Y. Zheng, X. G. Lei, B. S. Gao, Z. G. Wang, K. L. Wang, and X. F. He, *Phys. Rev. C* **90**, 024621 (2014).
- [6] G. S. Li, J. G. Wang, J. Lubian, H. O. Soler, Y. D. Fang, M. L. Liu, N. T. Zhang, X. H. Zhou, Y. H. Zhang, B. S. Gao, Y. H. Qiang, S. Guo, S. C. Wang, K. L. Wang, K. K. Zheng, R. Li, and Y. Zheng, *Phys. Rev. C* **100**, 054601 (2019).
- [7] M. Kaushik, G. Gupta, S. Thakur, H. Krishnamoorthy, P. P. Singh, V. V. Parkar, V. Nanal, A. Shrivastava, R. G. Pillay, K. Mahata, K. Ramachandran, S. Pal, C. S. Palshetkar, and S. K. Pandit, *Phys. Rev. C* **101**, 034611 (2020).
- [8] M. Dasgupta, D. J. Hinde, S. L. Sheehy, and B. Bouriquet, *Phys. Rev. C* **81**, 024608 (2010).
- [9] R. Anjos, C. Muri, J. Lubian, P. Gomes, I. Padron, J. Alves, G. Martí, J. Fernández Niello, A. Pacheco, O. Capurro *et al.*, *Phys. Lett. B* **534**, 45 (2002).
- [10] M. Hugi, J. Lang, R. Müller, E. Ungricht, K. Bodek, L. Jarczyk, B. Kamys, A. Magiera, A. Strzałkowski, and G. Willim, *Nucl. Phys. A* **368**, 173 (1981).
- [11] S. B. Moraes, P. R. S. Gomes, J. Lubian, J. J. S. Alves, R. M. Anjos, M. M. Sant'Anna, I. Padrón, C. Muri, R. Liguori Neto, and N. Added, *Phys. Rev. C* **61**, 064608 (2000).
- [12] Y. D. Fang, P. R. S. Gomes, J. Lubian, M. L. Liu, X. H. Zhou, D. R. Mendes Junior, N. T. Zhang, Y. H. Zhang, G. S. Li, J. G. Wang, S. Guo, Y. H. Qiang, B. S. Gao, Y. Zheng, X. G. Lei, and Z. G. Wang, *Phys. Rev. C* **91**, 014608 (2015).
- [13] V. Jha, V. V. Parkar, and S. Kailas, *Phys. Rev. C* **89**, 034605 (2014).
- [14] V. V. Parkar, V. Jha, S. K. Pandit, S. Santra, and S. Kailas, *Phys. Rev. C* **87**, 034602 (2013).
- [15] H. Kumawat, V. Jha, V. V. Parkar, B. J. Roy, S. K. Pandit, R. Palit, P. K. Rath, C. S. Palshetkar, S. K. Sharma, S. Thakur, A. K. Mohanty, A. Chatterjee, and S. Kailas, *Phys. Rev. C* **86**, 024607 (2012).
- [16] M. Dasgupta, P. R. S. Gomes, D. J. Hinde, S. B. Moraes, R. M. Anjos, A. C. Berriman, R. D. Butt, N. Carlin, J. Lubian, C. R. Morton, J. O. Newton, and A. Szanto de Toledo, *Phys. Rev. C* **70**, 024606 (2004).
- [17] P. Descouvemont, T. Druet, L. F. Canto, and M. S. Hussein, *Phys. Rev. C* **91**, 024606 (2015).
- [18] P. Descouvemont and N. Itagaki, *Phys. Rev. C* **97**, 014612 (2018).
- [19] C. Signorini, A. Andrighetto, J. Guo, M. Ruan, L. Stroe, F. Soramel, K. Löbner, L. Müller, D. Pierroutsakou, M. Romoli *et al.*, *Nucl. Phys. A* **701**, 23 (2002).
- [20] M. S. Zisman, J. G. Cramer, D. A. Goldberg, J. W. Watson, and R. M. DeVries, *Phys. Rev. C* **21**, 2398 (1980).
- [21] C. S. Palshetkar, S. Santra, A. Shrivastava, A. Chatterjee, S. K. Pandit, K. Ramachandran, V. V. Parkar, V. Nanal, V. Jha, B. J. Roy, and S. Kailas, *Phys. Rev. C* **89**, 064610 (2014).
- [22] M. A. G. Alvarez, M. Rodríguez-Gallardo, J. P. Fernández-García, J. Casal, and J. A. Lay, *Phys. Rev. C* **103**, 054614 (2021).
- [23] J. Lei and A. M. Moro, *Phys. Rev. C* **95**, 044605 (2017).
- [24] A. Pakou, N. Alamanos, A. Gillibert, M. Kokkoris, S. Kossionides, A. Lagoyannis, N. G. Nicolis, C. Papachristodoulou, D. Patriris, D. Pierroutsakou *et al.*, *Phys. Rev. Lett.* **90**, 202701 (2003).
- [25] S. B. Gazes, J. E. Mason, R. B. Roberts, and S. G. Teichmann, *Phys. Rev. Lett.* **68**, 150 (1992).
- [26] R. J. Woolliscroft, N. M. Clarke, B. R. Fulton, R. L. Cowin, M. Dasgupta, D. J. Hinde, C. R. Morton, and A. C. Berriman, *Phys. Rev. C* **68**, 014611 (2003).
- [27] C. Castaneda, H. Smith, P. Singh, J. Jastrzebski, H. Karwowski, and A. Gaigalas, *Phys. Lett. B* **77**, 371 (1978).
- [28] J. Lei and A. M. Moro, *Phys. Rev. Lett.* **122**, 042503 (2019).
- [29] S. K. Pandit, A. Shrivastava, K. Mahata, N. Keeley, V. V. Parkar, R. Palit, P. C. Rout, K. Ramachandran, A. Kumar, S. Bhattacharyya *et al.*, *Phys. Lett. B* **820**, 136570 (2021).
- [30] K. J. Cook, E. C. Simpson, L. T. Bezzina, M. Dasgupta, D. J. Hinde, K. Banerjee, A. C. Berriman, and C. Sengupta, *Phys. Rev. Lett.* **122**, 102501 (2019).
- [31] A. Diaz-Torres, D. J. Hinde, J. A. Tostevin, M. Dasgupta, and L. R. Gasques, *Phys. Rev. Lett.* **98**, 152701 (2007).
- [32] D. Gupta, C. Samanta, R. Kanungo, M. Sharan, S. Kailas, A. Chatterjee, K. Mahata, and A. Shrivastava, *Nucl. Phys. A* **646**, 161 (1999).
- [33] A. Chatterjee, LAMPS: Linux Advanced Multiparameter System (2008), <http://www.tifr.res.in/~pell/lamps.html>.
- [34] H. Kumawat, V. Jha, V. V. Parkar, B. J. Roy, S. Santra, V. Kumar, D. Dutta, P. Shukla, L. M. Pant, A. K. Mohanty,



- R. K. Choudhury, and S. Kailas, *Phys. Rev. C* **81**, 054601 (2010).
- [35] J. Schiffer, H. Körner, R. Siemssen, K. Jones, and A. Schwarzschild, *Phys. Lett. B* **44**, 47 (1973).
- [36] W. Henning, Y. Eisen, H.-J. Körner, D. G. Kovar, J. P. Schiffer, S. Vigdor, and B. Zeidman, *Phys. Rev. C* **17**, 2245 (1978).
- [37] A. Gavron, *Phys. Rev. C* **21**, 230 (1980).
- [38] A. V. Ignatyuk, G. N. Smirenkin, and A. S. Tishin, *Yad. Fiz.* **21**, 485 (1975) [*Sov. J. Nucl. Phys.* **21**, 255 (1975)].
- [39] C. Joshi, H. Kumawat, V. V. Parkar, D. Dutta, S. V. Suryanarayana, V. Jha, R. K. Singh, N. L. Singh, and S. Kailas, *Phys. Rev. C* **105**, 034615 (2022).
- [40] I. J. Thompson, FRESKO (2019), version FRES 3.3, <http://www.fresco.org.uk/source/fres-v31.html>.
- [41] Y. Xu, Y. Han, H. Liang, Z. Wu, H. Guo, and C. Cai, *Phys. Rev. C* **99**, 034618 (2019).
- [42] I. J. Thompson, *Comput. Phys. Rep.* **7**, 167 (1988).
- [43] F. Ajzenberg-Selove and T. Lauritsen, *Nucl. Phys. A* **227**, 1 (1974).
- [44] N. Keeley, K. W. Kemper, and K. Rusek, *Phys. Rev. C* **64**, 031602(R) (2001).
- [45] V. Avrigeanu, M. Avrigeanu, and C. Mănăilescu, *Phys. Rev. C* **90**, 044612 (2014).
- [46] J. Lang, R. Müller, J. Unternährer, L. Jarczyk, B. Kamys, and A. Strzalkowski, *Phys. Rev. C* **16**, 1448 (1977).
- [47] A. Koning and J. Delaroche, *Nucl. Phys. A* **713**, 231 (2003).
- [48] O. Karban, J. England, D. Barker, M. Mannion, J. Nelson, C. Ogilvie, L. Potvin, L. Zybert, R. Zybert, N. Clarke *et al.*, *Nucl. Phys. A* **472**, 189 (1987).
- [49] F. Pellegrini, I. Filosofo, M. I. El Zaiki, and I. Gabrielli, *Phys. Rev. C* **8**, 1547 (1973).
- [50] Z. H. Li, Y. J. Li, J. Su, B. Guo, E. T. Li, K. J. Dong, X. X. Bai, Z. C. Li, J. C. Liu, S. Q. Yan, Y. B. Wang, S. Zeng, G. Lian, B. X. Wang, S. J. Jin, X. Liu, W. J. Zhang, W. Z. Huang, Q. W. Fan, L. Gan, Z. D. Wu, and W. P. Liu, *Phys. Rev. C* **87**, 017601 (2013).
- [51] Y. Xu, Y. Han, J. Hu, H. Liang, Z. Wu, H. Guo, and C. Cai, *Phys. Rev. C* **97**, 014615 (2018).
- [52] F. Ajzenberg-Selove, *Nucl. Phys. A* **490**, 1 (1988).
- [53] Y.-L. Xu, H.-R. Guo, Y.-L. Han, and Q.-B. Shen, *Int. J. Mod. Phys. E* **27**, 1850099 (2018).